

AperTO - Archivio Istituzionale Open Access dell'Università di Torino

Radial velocity confirmation of K2-100b: A young, highly irradiated, and low-density transiting hot Neptune

This is the author's manuscript

Original Citation:

Availability:

This version is available <http://hdl.handle.net/2318/1731241> since 2020-02-26T12:37:05Z

Published version:

DOI:10.1093/mnras/stz2569

Terms of use:

Open Access

Anyone can freely access the full text of works made available as "Open Access". Works made available under a Creative Commons license can be used according to the terms and conditions of said license. Use of all other works requires consent of the right holder (author or publisher) if not exempted from copyright protection by the applicable law.

(Article begins on next page)

Radial velocity confirmation of K2-100b: a young, highly irradiated, and low density transiting hot Neptune

O. Barragán^{1,*}, S. Aigrain¹, D. Kubyskhina², D. Gandolfi³, J. Livingston⁴, M. C. V. Fridlund^{5,6}, L. Fossati², J. Korth⁷, H. Parviainen^{8,9}, L. Malavolta¹⁰, E. Pallé^{8,9}, H. J. Deeg^{8,9}, G. Nowak^{8,9}, V. M. Rajpaul¹¹, N. Zicher¹, G. Antoniciello¹², N. Narita^{13,14,15,8}, S. Albrecht¹⁶, L. R. Bedin¹⁷, J. Cabrera¹⁸, W. D. Cochran¹⁹, J. de Leon⁴, Ph. Eig Müller¹⁸, A. Fukui²⁰, V. Granata¹², S. Grziwa⁷, E. Guenther²¹, A. P. Hatzes²¹, N. Kusakabe^{13,15}, D. W. Latham²², M. Libralato²³, R. Luque^{8,9}, P. Montañés-Rodríguez^{8,9}, F. Murgas^{8,9}, D. Nardiello¹², I. Pagano¹⁰, G. Piotto¹², C. M. Persson^{5,6}, S. Redfield²⁴, and M. Tamura^{4,13,15}

¹Sub-department of Astrophysics, Department of Physics, University of Oxford, Oxford, OX1 3RH, UK

²Space Research Institute, Austrian Academy of Sciences, Schmiedlstrasse 6, A-8041 Graz, Austria

³Dipartimento di Fisica, Università di Torino, via P. Giuria 1, 10125 Torino, Italy

⁴Department of Astronomy, University of Tokyo, 7-3-1 Hongo, Bunkyo-ku, Tokyo 113-0033, Japan

⁵Department of Earth and Space Sciences, Chalmers University of Technology, Onsala Space Observatory, 439 92 Onsala, Sweden

⁶Leiden Observatory, University of Leiden, PO Box 9513, 2300 RA, Leiden, The Netherlands

⁷Rheinisches Institut für Umweltforschung an der Universität zu Köln, Aachener Strasse 209, 50931 Köln

⁸Instituto de Astrofísica de Canarias, 38205 La Laguna, Tenerife, Spain

⁹Departamento de Astrofísica, Universidad de La Laguna, 38206 La Laguna, Tenerife, Spain

¹⁰INAF - Osservatorio Astrofisico di Catania, Via S. Sofia 78, 95123 Catania, Italy

¹¹Astrophysics Group, Cavendish Laboratory, University of Cambridge, J. J. Thomson Avenue, Cambridge CB3 0HE, UK

¹²Dipartimento di Fisica e Astronomia "Galileo Galilei", Università di Padova, Vicolo dell'Osservatorio 3, 35122, Padova, Italy

¹³Astrobiology Center, 2-21-1 Osawa, Mitaka, Tokyo 181-8588, Japan

¹⁴JST, PRESTO, 2-21-1 Osawa, Mitaka, Tokyo 181-8588, Japan

¹⁵National Astronomical Observatory of Japan, 2-21-1 Osawa, Mitaka, Tokyo 181-8588, Japan

¹⁶Stellar Astrophysics Centre, Department of Physics and Astronomy, Aarhus University, Ny Munkegade 120, DK-8000 Aarhus C, Denmark

¹⁷INAF - Osservatorio Astronomico di Padova, Vicolo dell'Osservatorio 5, Padova, IT-3512, Italy

¹⁸Institute of Planetary Research, German Aerospace Center, Rutherfordstrasse 2, 12489 Berlin, Germany

¹⁹Department of Astronomy and McDonald Observatory, University of Texas at Austin, 2515 Speedway, Stop C1400, Austin, TX 78712, USA

²⁰Department of Earth and Planetary Science, The University of Tokyo, 7-3-1 Hongo, Bunkyo-ku, Tokyo 113-0033, Japan

²¹Thüringer Landessternwarte Tautenburg, Sternwarte 5, 07778 Tautenburg, Germany

²²Center for Astrophysics, Harvard & Smithsonian, 60 Garden Street, Cambridge, MA 02138, USA

²³Space Telescope Science Institute, 3700 San Martin Drive, Baltimore, MD 21218, USA

²⁴Astronomy Department and Van Vleck Observatory, Wesleyan University, Middletown, CT 06459, USA

Last updated 2015 May 22; in original form 2013 September 5

ABSTRACT

We present a detailed analysis of HARPS-N radial velocity observations of K2-100, a young and active star in the Praesepe cluster, which hosts a transiting planet with a period of 1.7 days. We model the activity-induced radial velocity variations of the host star with a multi-dimensional Gaussian Process framework and detect a planetary signal of $10.6 \pm 3.0 \text{ m s}^{-1}$ which matches the transit ephemeris, and translates to a planet mass of $21.8 \pm 6.2 M_{\oplus}$. We perform a suite of validation tests to confirm that our detected signal is genuine. This is the first mass measurement for a transiting planet in a young open cluster. The relatively low density of the planet, $2.04^{+0.66}_{-0.61} \text{ g cm}^{-3}$, implies that K2-100b retains a significant volatile envelope. We estimate that the planet is losing its atmosphere at a rate of $10^{11} - 10^{12} \text{ g s}^{-1}$ due to the high level of radiation it receives from its host star.

Key words: planetary systems — planets and satellites: individual: K2-100b

1 INTRODUCTION

Theoretical evolution models predict that the most significant changes in the bulk and orbital parameters of exoplanets occur in the first few hundred Myr of their evolution (e.g., Adams & Laughlin 2006; Kubyskhina et al. 2018a; Raymond et al. 2009). Planets orbiting stars in young open clusters are thus particularly valuable tests of these models. The exquisite photometry collected by the *K2* space mission (Howell et al. 2014) and its observing strategy focused on the Ecliptic plane have enabled the detection of the first transiting planet candidates in star forming regions and young stars (e.g., David et al. 2016a,b, 2019; Libralato et al. 2016; Mann et al. 2016a,b, 2017, 2018; Pepper et al. 2017; Livingston et al. 2018a, 2019), but none so far has mass measurements. Recent studies show that these young transiting exoplanets seem to be larger than their counterparts with similar periods orbiting more evolved stars (Mann et al. 2016b). This suggests that photoevaporation by the host star plays an important role in shaping the planet atmosphere in the first few Gyr (as predicted by e.g., Owen & Wu 2013). However, expected evaporation rates depend strongly on planet mass, so measuring masses for these young transiting planets is important to test this scenario further.

This paper presents the first firm RV confirmation of a transiting planet in a young open cluster. K2-100 (EPIC 211990866, $\alpha_{J2000} = 08:38:24.30$, $\delta_{J2000} = +20:06:21.83$) is a bright ($V = 10.52$ mag) G-dwarf member (Kraus & Hillenbrand 2007) of the Praesepe cluster (NGC 2632, M44), which has an estimated age of 700–800 Myr and distance of ~ 180 pc (Brandt & Huang 2015; Bossini et al. 2019; Salaris et al. 2004; van Leeuwen 2009). The transits of K2-100b, were discovered independently by Pope et al. (2016) and Mann et al. (2017, hereafter M17) in *K2* campaign 5 data, though only the latter identified the host star as a Praesepe member. Analysis of the *K2* light curve alongside optical and infrared spectroscopy and adaptive optics imaging enabled M17 to rule out most false positive scenarios and statistically validate the planetary nature of K2-100b, alongside 6 other Praesepe candidates orbiting fainter stars. With a period of 1.67 d and ~ 800 ppm transits, which implies a planet radius of $\sim 3.8 R_{\oplus}$, K2-100b is a hot Neptune, and its bright host star made it a good candidate for further characterisation.

The RV follow-up of planets in young open clusters is challenging because their host stars rotate rapidly and are magnetically active. This gives rise to quasi-periodic variations in the apparent stellar RV, which can be very difficult to disentangle from the planetary signal(s). Gaussian Process Regression (GPR) can be used to model activity signals in RV data (see e.g. Haywood et al. 2014; Grunblatt et al. 2015). This approach is even more powerful when complementary activity indicators extracted from the spectra are modelled alongside the RVs, as in the framework developed by Rajpaul et al. (2015, hereafter R15). In this paper, we used the framework of R15 to analyse RV observations of K2-100 and detect the reflex motion of the star induced by the transiting planet at the $> 3\sigma$ level, despite the fact that the latter is of considerably lower amplitude than the activity-induced variations.

2 OBSERVATIONS

2.1 Photometry

K2 observed K2-100 as part of its Campaign 5 (C5, 2015-04-27 UTC to 2015-07-10 UTC) in long-cadence mode (30 min). This star was re-observed by *K2* in short cadence (1 min) mode on

its Campaign 18 (C18, 2018-05-12 UTC to 2018-07-02 UTC). We downloaded the K2SFF (Vanderburg & Johnson 2014) light curve for C5 from the Mikulski Archive for Space Telescopes (<https://archive.stsci.edu/k2/>). We used the *lightkurve* package (Lightkurve Collaboration et al. 2018) to obtain the C18 *K2* light curve. We corrected for systematics using the pixel level decorrelation (PLD) as implemented in the *lightkurve* package.

Stefansson et al. (2018) performed a ground-based photometric follow-up of K2-100. They used the Engineered Diffuser instrument on the Astrophysical Research Council Telescope Imaging Camera (ARCTIC) imager located at the ARC 3.5 m Telescope at Apache Point Observatory. We downloaded the available public light curve from the online version of Stefansson et al. (2018) to use it in the analysis presented in Sect. 3.5.

We observed three transits of K2-100 with the MuSCAT2 multicolour photometer (Narita et al. 2019) installed in the Carlos Sanchez Telescope (TCS) in the Teide observatory on the nights of 2018-12-28 UTC, 2019-01-02 UTC, and 2019-01-22 UTC. All observations covered from 2 to 3.2 hours around the expected mid-transit time, and were carried simultaneously in the r' , i' , and z' passbands with a common exposure time of 10 seconds. The photometry was done with the MuSCAT2 pipeline based on PyTransit (Parviainen 2015) and LDTk (Parviainen & Aigrain 2015).

We searched for transit timing variations (TTVs) using PyTV (Python Tool for Transit Variations, Korth 2019, in prep.). We detected no TTVs; therefore, our results are consistent with a constant period model. This result, together with the precise ephemeris, implies that K2-100 can be efficiently scheduled for future follow-up observations.

2.2 Spectroscopy

We acquired 78 high-resolution ($R \approx 115\,000$) spectra of K2-100 with the HARPS-N spectrograph mounted at the 3.58-m Telescopio Nazionale Galileo at Roque de Los Muchachos observatory (La Palma, Spain), as part of the observing programs CAT15B_35 (PI: Deeg), CAT15B_79 (PI: Palle), and ITP16_6 (PI: Malavolta). We processed the data using the dedicated HARPS-N pipeline and extracted the RVs by cross-correlating the HARPS-N spectra with a G2 numerical mask. We also extracted the Ca II activity indicator $\log R'_{\text{HK}}$ assuming a $B-V = 0.583$. Table A1 reports the HARPS-N RVs and their uncertainties along with the full-width at half maximum (FWHM) and the bisector inverse slope (BIS) of the cross-correlation function (CCF), $\log R_{\text{HK}}$, and the signal-to-noise ratio (S/N) per pixel at 5500 Å. For the analysis presented in Sect. 3.5, we removed 5 RV data points with a relative low signal-to-noise ($S/N < 12$).

3 DATA ANALYSIS

3.1 Stellar parameters

We determined the spectroscopic parameters of K2-100 from the co-added HARPS-N spectrum using the software Spectroscopy Made Easy (SME, version 5.22; Piskunov & Valenti 2017; Valenti & Piskunov 1996) along with ATLAS12 model atmospheres (Kurucz 2013) and atomic/molecular parameters from the VALD database (Ryabchikova et al. 2015). The effective temperature T_{eff} , surface gravity $\log g_{\star}$, iron abundance [Fe/H], and projected rotational velocity $v \sin i_{\star}$ were measured following the same techniques described in, e.g., Fridlund et al. (2017), Gandolfi et al. (2017), and

Persson et al. (2018). The micro- (v_{mic}) and macro-turbulent (v_{mac}) velocities were fixed through the empirical calibration equations of Bruntt et al. (2010) and Doyle et al. (2014). As a sanity check, we also carried out an independent spectroscopic analysis using the package `specmatch-emp` (Yee et al. 2017). This code compares the observed spectrum with a library of ~ 400 FGKM template spectra and minimises the differences between the observed and the library data. The derived spectroscopic parameters agree within 1-sigma with those found by SME.

Following the method described in Gandolfi et al. (2008), we measured the interstellar extinction along the line of sight to the star and found that it is consistent with zero. We derived the stellar mass, radius, and age using the on-line interface PARAM-1.3 (<http://stev.oapd.inaf.it/cgi-bin/param>) and PARSEC stellar tracks and isochrones (Bressan et al. 2012), along with the visual magnitude ($V=10.56$; Mermilliod 1987), the GAIA parallax ($\pi=5.2645 \pm 0.0678$ mas; Gaia Collaboration et al. 2018), and our effective temperature and iron abundance measurements. The derived stellar parameters are listed in Table 1. We note that the inferred supersolar metallicity of K2-100 ($[\text{Fe}/\text{H}] = 0.22 \pm 0.09$) is consistent with previous values measured for Praesepe stars (Boesgaard et al. 2013; Pace et al. 2008).

3.2 Stellar density analysis

M17 and Livingston et al. (2018b) noticed that K2-100's stellar density coming from the light curve analysis (assuming a circular orbit) differs from that from the spectroscopic parameters. This could be explained by a mischaracterised host star or an eccentric orbit. We discard the possibility that the star is mischaracterised given that our independent stellar parameter estimation is in agreement with the values reported by M17 and Livingston et al. (2018b). We also discard a significantly eccentric orbit given that the circularisation time of K2-100b's orbit (≈ 20 Myr, following Jackson et al. 2008) is significantly smaller than the system age.

We found out that this discrepancy was caused by a wide posterior distribution for a/R_{\star} when analysing K2 C5 data only. Figure 1 shows the posterior distribution for the scaled semi-major axis, a/R_{\star} (that relates directly with stellar density, see e.g., Winn 2010), by fitting C5 K2 data only, C18 K2 data only, and also by fitting all available transits. We set uniform priors on a/R_{\star} for all cases. When fitting the C5 K2 data, the MCMC converges to a solution which produces a wide posterior for a/R_{\star} with median and 68% credible interval given by $7.40^{+0.70}_{-1.75}$. This solution translates to a stellar density of $2.73^{+0.85}_{-1.62} \text{ g cm}^{-3}$. These values are similar to the values reported by M17 and Livingston et al. (2018b). When fitting all available transits, the MCMC sampling converges to a narrower posterior distribution with an inferred value of $a/R_{\star} = 5.36^{+0.25}_{-0.20}$ (we note that this value is still inside the posterior distribution found by fitting only C5 K2 data). This value gives a stellar density of $\rho_{\star} = 1.04 \pm 0.15 \text{ g cm}^{-3}$ which is consistent with the value derived in Sect. 3.1 (see Fig. 1). We note that when fitting the C18 K2 alone we also get a a/R_{\star} which is consistent with the expected value of a/R_{\star} from Kepler's third law and the stellar parameters derived in Sect. 3.1. The new analysis including all available transits suggests that the planetary orbit is nearly circular, therefore we assume a circular orbit for K2-100b's in the rest of the manuscript. In order to speed-up convergence for the final analysis presented in Sect. 3.5, we used the derived stellar parameters and Kepler's third law to set a Gaussian prior on a/R_{\star} (see Fig. 1).

We note that the inferred a/R_{\star} has a direct effect on the ge-

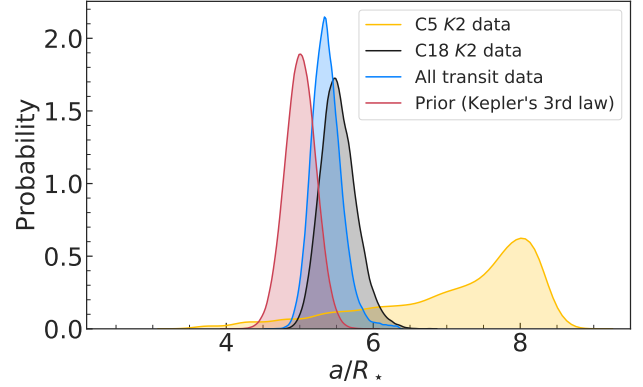


Figure 1. Posterior distribution for a/R_{\star} for different analyses. The posterior distribution for a/R_{\star} fitting only K2 C5 data and K2 C18 data are shown in yellow and black, respectively. Blue shows the posterior distribution for a/R_{\star} fitting all available transits. We also show the prior on a/R_{\star} using the derived stellar parameters in Sect. 3.1 and the planetary orbital period in red.

Table 1. Stellar parameters.

Parameter	Value	Source
Stellar mass M_{\star} (M_{\odot})	1.15 ± 0.05	This work
Stellar radius R_{\star} (R_{\odot})	1.24 ± 0.05	This work
$v \sin i_{\star}$ (km s^{-1})	14 ± 2	This work
Stellar density ρ_{\star} (g cm^{-3})	$0.85^{+0.12}_{-0.10}$	This work
Effective Temperature T_{eff} (K)	5945 ± 110	This work
Surface gravity $\log g_{\star}$ (cgs)	4.33 ± 0.10	This work
Iron abundance $[\text{Fe}/\text{H}]$ (dex)	0.22 ± 0.09	This work
Star age (Myr)	750^{+4}_{-7}	B19
Spectral type	G0V	PM13

Note: B19 - Bossini et al. (2019), PM13 - Pecauc & Mamajek (2013).

ometry on the system. For instance, the orbital inclination, planet radius, and other derived quantities differ from those reported in M17 and Livingston et al. (2018b).

3.3 Planet validation

K2-100b was first validated by Mann et al. (2017), who computed a false-positive probability (FPP) of 0.36% using the `vespa` software package (Morton 2012). Livingston et al. (2018b) subsequently analysed the K2 data (as processed by `k2phot`; Petigura et al. 2015) and obtained a slightly higher FPP of 1.2%, just above their validation threshold of 1%. This disagreement in FPP is comparatively small, and likely results from the use of different photometric pipelines, as well as stellar parameter estimates. We have used the new information contained in the short cadence K2 C18 photometry of K2-100 and our simultaneous multi-band MuSCAT2 photometry to revisit the FPP of K2-100b. The short cadence K2 data put tighter constraints on the transit shape than was possible with the long cadence data from C5, which in turn has a significant impact on the FPP. We now obtain an extremely low FPP of $\lesssim 10^{-6}$ for K2-100b using `vespa`.

We can also independently constrain the possibility of various false positive scenarios by measuring $r_p \equiv R_p/R_{\star}$ in different bandpasses (see e.g., Parviainen et al. 2019). We performed a fit to all our available flattened transits allowing for a free r_p for

each band with uniform priors between $[0, 0.05]$. We got $r_{p,K2} = 0.0286 \pm 0.0003$, $r_{p,ARCTIC} = 0.0308 \pm 0.0011$, $r_{p,r} = 0.0241 \pm 0.0015$, $r_{p,i} = 0.0263 \pm 0.0015$, $r_{p,z} = 0.0281 \pm 0.0019$; the agreement of r_p in these bandpasses is inconsistent with most false positive scenarios, thus confirming the *vespa* result.

3.4 RV analysis using multi-dimensional GP

In this work we use the GP framework presented by R15 to model the RV data along with the $\log R'_{\text{HK}}$ and BIS. Briefly, this approach assumes that all stellar activity signals can be modelled by the same latent variable $G(t)$ (and its derivatives) which is described by a zero-mean GP and a covariance function γ . Following R15, the RV, $\log R'_{\text{HK}}$ and BIS time-series can be modelled as

$$\begin{aligned} \Delta RV &= V_c G(t) + V_r \dot{G}(t), \\ \log R'_{\text{HK}} &= L_c G(t), \\ \text{BIS} &= B_c G(t) + B_r \dot{G}(t), \end{aligned} \quad (1)$$

respectively. The variables V_c , V_r , L_c , B_c and B_r are free parameters which relate the individual time series to an underlying Gaussian Process $G(t)$. The GP itself is a latent (unobserved) variable, which can be loosely interpreted as representing the projected area of the visible stellar disc that is covered in spots or active regions at a given time. The GP is assumed to have zero mean and covariance matrix \mathbf{K} , where $K_{ij} = \gamma(t_i, t_j)$. Following R15, we adopt the quasi-periodic covariance function

$$\gamma(t_i, t_j) = \exp \left[-\frac{\sin^2[\pi(t_i - t_j)/P_{\text{GP}}]}{2\lambda_p^2} - \frac{(t_i - t_j)^2}{2\lambda_e^2} \right], \quad (2)$$

where P_{GP} is the period of the activity signal, λ_p the inverse of the harmonic complexity, and λ_e is the long term evolution timescale. This choice of covariance function is widely used to model stellar activity signals in both photometry and RVs (see e.g. Aigrain et al. 2012; Haywood et al. 2014 and R15). The full expressions for the covariance between the three types of observations are given in R15.

3.5 RV and transit modelling

We used the open source code `pyaneti` (Barragán et al. 2019) to model the light curve and RV data. We modified `pyaneti`'s public version to allow for multi-band transit and GP analyses. We also implemented the multi-dimensional GP approach described in Sect. 3.4 and R15.

We used `exotrending` (Barragán & Gandolfi 2017) to isolate each transit and to remove long term trends in the light curves as described in Barragán et al. (2018a,b). We re-sampled the model over ten steps to account for the long-cadence (30min, C5) K2 data (Kipping 2010). We did not re-sample the model for K2 and ground-based short-cadence data. We assumed that the difference of transit depth between different bands is negligible; therefore, we fit for a single radius ratio R_p/R_\star for all the bands. We fitted for the limb darkening parameters for each band using uniform priors and the parametrisation described by Kipping (2013). We have assumed a circular orbit (See Sect. 3.2).

We performed a joint fit of all transits together with the RV, $\log R'_{\text{HK}}$, and BIS time-series using the approach presented in Sect. 3.4. A summary of the fitted parameters and priors are presented in Table 2. We used 500 chains to sample the parameter space (38 free parameters). For the burning-in phase we used the last 5000 of converged chains with a thin factor of 10, leading to a final number of 250,000 independent points for each fitted parameter.

4 RESULTS AND DISCUSSION

Figure 2 shows the RV, $\log R'_{\text{HK}}$ and BIS time-series together with the inferred models. We also show the phase-folded RV and transit models, along with the data points in Figures 3 and 4, respectively. We inferred a planetary induced RV semi-amplitude of $10.6 \pm 3.0 \text{ m s}^{-1}$, which translates into a planet mass of $21.8 \pm 6.2 M_\oplus$. Other parameter estimates are presented in Table 2.

We note that we also analysed the RV data set with standard RV analysis techniques, such as Fourier decomposition (e.g., Barragán et al. 2018a; Pepe et al. 2013) and GPs trained with photometry (e.g., Barragán et al. 2018b; Malavolta et al. 2018). We found hints of the induced Doppler signal with a significance $\lesssim 2$ -sigma. This shows that the simultaneous regression of the activity/asymmetry indicators play a fundamental role to measure the Doppler semi-amplitude with higher precision.

As a first check of the validity of our detection, we compare the Bayesian Information Criteria (BIC; see e.g., Burnham & Anderson 2002). We repeated the analysis presented in Sect. 3.5 by fitting a model with and without planet. We model only the RV-related time-series, i.e., with no transit modelling. For the fit with planet, we set priors on the ephemeris coming from the transit analysis. We conclude that the model including the planet signal is strongly preferred over the model without it with a $\Delta\text{BIC} = 26$.

Rajpaul et al. (2016) showed that spurious RV detection of planets around active stars can arise due to a combination of complex activity models and the window function of the observations. To check that this is not the case here, we created 250 synthetic RV, $\log R'_{\text{HK}}$, and BIS time-series using the best-fit GP model, with no planet in the RV data set. We added white noise to each point from a Gaussian distribution with standard deviation as the nominal error bar of each data point. We ran an MCMC fit as the one described in Sect. 3.5 (without transit data) for each data set, allowing for an RV signal with priors on the ephemeris of the planet. These simulations give rise to a "detection" (we define a "detection" as a signal with a significance > 2 -sigma) only in 0.4% of the cases. We then repeat the experiment creating 250 more mock data sets, but this time injecting a coherent signal with an amplitude of 10 m s^{-1} in the RV data set and same ephemeris as K2-100b. For this case we have a "detection" on 90% of the runs. These results suggest that the planetary signal we detected in the real data is genuine.

As a further test of the reliability of our detection, we also extracted the RV measurements with a K5 numerical mask, and repeated the analysis presented in Sect. 3.5. We found an amplitude of $K = 12.4 \pm 3.5 \text{ m s}^{-1}$ which is within 1σ of the value obtained with the RVs extracted using the fiducial G2 mask.

Figure 5 shows a planet density vs insolation plot for small planets ($R_p < 4 R_\oplus$) with masses measured to better than 50% as listed in the TEPICAT catalogue (Southworth 2011, <http://www.astro.keele.ac.uk/jkt/tepicat/>). The plot also shows the limit of $650 F_\oplus$ given by Lundkvist et al. (2016) likely related to the presence/lack of a hydrogen-dominated atmosphere as a consequence of strong atmospheric escape. We find that for weakly irradiated planets ($< 650 F_\oplus$), low (sub-Earth) densities are common, in contrast to highly irradiated for which most of the planets have densities equal or larger than that of the Earth, with only two exceptions: NGTS-4b (West et al. 2019) and K2-100b. We discuss in more detail these two planets below.

Figure 6 shows the position of K2-100b in a mass-radius diagram together with two-layer composition models by Zeng et al. (2016). With a mass of $21.8 \pm 6.2 M_\oplus$, a radius of $3.88 \pm 0.16 R_\oplus$, and a density of $2.04_{-0.61}^{+0.66} \text{ g cm}^{-3}$, we expect that K2-100b is a planet

Table 2. K2-100b parameters.

Parameter	Prior ^(a)	Value ^(b)
Model Parameters for K2-100b		
Orbital period P_{orb} (days)	$\mathcal{U}[1.6737, 1.6740]$	1.6739035 ± 0.0000004
Transit epoch T_0 (BJD - 2,450,000)	$\mathcal{U}[7140.70, 7140.75]$	7140.71941 ± 0.00027
e	$\mathcal{F}[0]$	0
ω_{\star}	$\mathcal{F}[\pi/2]$	$\pi/2$
Scaled semi-major axis a/R_{\star}	$\mathcal{N}[5.01, 0.21]$	5.21 ± 0.13
Scaled planetary radius R_p/R_{\star}	$\mathcal{U}[0, 0.05]$	0.02867 ± 0.00028
Impact parameter, b	$\mathcal{U}[0, 1]$	0.791 ± 0.014
Radial velocity semi-amplitude variation K (m s^{-1})	$\mathcal{U}[0, 50]$	10.6 ± 3.0
GP Period P_{GP} (days)	$\mathcal{U}[4, 5.1]$	4.315 ± 0.014
λ_p	$\mathcal{U}[0.1, 2]$	$0.558^{+0.082}_{-0.069}$
λ_c	$\mathcal{U}[1, 300]$	$31.2^{+7.6}_{-6.3}$
V_c (km s^{-1})	$\mathcal{U}[0, 0.1]$	$0.0058^{+0.0049}_{-0.0037}$
V_r (km s^{-1})	$\mathcal{U}[-1, 1]$	$0.0421^{+0.0147}_{-0.0095}$
L_c	$\mathcal{U}[0, 1]$	$0.0242^{+0.0079}_{-0.0055}$
B_c (km s^{-1})	$\mathcal{U}[-1.5, 1.5]$	$0.020^{+0.061}_{-0.059}$
B_r (km s^{-1})	$\mathcal{U}[-0.5, 0.5]$	$-0.086^{+0.037}_{-0.049}$
Offset HARPS-N (km s^{-1})	$\mathcal{U}[34.1998, 34.5825]$	34.393 ± 0.003
Offset $\log R'_{\text{HK}}$	$\mathcal{U}[-4.5878, -4.2885]$	-4.45 ± 0.01
Offset BIS (km s^{-1})	$\mathcal{U}[-1.5568, 0.6372]$	-0.04 ± 0.04
Jitter term $\sigma_{\text{HARPS-N}}$ (m s^{-1})	$\mathcal{U}[0, 100]$	$2.60^{+3.15}_{-2.05}$
Jitter term $\sigma_{\log R'_{\text{HK}}}$	$\mathcal{U}[0, 1]$	0.0030 ± 0.0021
Jitter term BIS (m s^{-1})	$\mathcal{U}[0, 1000]$	291^{+27}_{-24}
Limb darkening q_1 for K2 C5	$\mathcal{U}[0, 1]$	$0.27^{+0.08}_{-0.07}$
Limb darkening q_2 for K2 C5	$\mathcal{U}[0, 1]$	$0.13^{+0.19}_{-0.10}$
Limb darkening q_1 for K2 C18	$\mathcal{U}[0, 1]$	$0.27^{+0.08}_{-0.07}$
Limb darkening q_2 for K2 C18	$\mathcal{U}[0, 1]$	$0.13^{+0.19}_{-0.07}$
Limb darkening q_1 for ARCTIC	$\mathcal{U}[0, 1]$	$0.03^{+0.06}_{-0.02}$
Limb darkening q_2 for ARCTIC	$\mathcal{U}[0, 1]$	$0.40^{+0.36}_{-0.28}$
Limb darkening q_1 for MUSCAT2 r'	$\mathcal{U}[0, 1]$	$0.73^{+0.19}_{-0.26}$
Limb darkening q_2 for MUSCAT2 r'	$\mathcal{U}[0, 1]$	$0.49^{+0.13}_{-0.15}$
Limb darkening q_1 for MUSCAT2 i'	$\mathcal{U}[0, 1]$	$0.57^{+0.27}_{-0.26}$
Limb darkening q_2 for MUSCAT2 i'	$\mathcal{U}[0, 1]$	$0.47^{+0.22}_{-0.23}$
Limb darkening q_1 for MUSCAT2 z'	$\mathcal{U}[0, 1]$	$0.73^{+0.19}_{-0.26}$
Limb darkening q_2 for MUSCAT2 z'	$\mathcal{U}[0, 1]$	$0.47^{+0.22}_{-0.23}$
Jitter term σ_{K2C5} ($\times 10^{-6}$)	$\mathcal{U}[0, 1 \times 10^3]$	40 ± 4
Jitter term σ_{K2C18} ($\times 10^{-6}$)	$\mathcal{U}[0, 1 \times 10^3]$	52 ± 4
Jitter term σ_{ARCTIC} ($\times 10^{-6}$)	$\mathcal{U}[0, 1 \times 10^3]$	267 ± 50
Jitter term $\sigma_{\text{MUSCAT2}r'}$ ($\times 10^{-6}$)	$\mathcal{U}[0, 1 \times 10^5]$	1321 ± 27
Jitter term $\sigma_{\text{MUSCAT2}i'}$ ($\times 10^{-6}$)	$\mathcal{U}[0, 1 \times 10^5]$	1419 ± 30
Jitter term $\sigma_{\text{MUSCAT2}z'}$ ($\times 10^{-6}$)	$\mathcal{U}[0, 1 \times 10^5]$	1919 ± 38
<i>Derived parameters</i>		
Planet mass (M_{\oplus})	...	21.8 ± 6.2
Planet radius (R_{\oplus})	...	3.88 ± 0.16
Planet density (g cm^{-3})	...	$2.04^{+0.66}_{-0.61}$
semi-major axis a (AU)	...	0.0301 ± 0.0014
Orbital inclination i (deg)	...	81.27 ± 0.37
Equilibrium temperature ^(c) T_{eq} (K)	...	1841 ± 41
Insolation F_p (F_{\oplus})	...	1915^{+178}_{-165}
Planet surface gravity ^(d) (cm s^{-2})	...	1536^{+436}_{-442}
Planet surface gravity (cm s^{-2})	...	1421^{+427}_{-413}

Note – ^(a) $\mathcal{U}[a, b]$ refers to uniform priors between a and b , $\mathcal{N}[a, b]$ to Gaussian priors with median a and standard deviation b , and $\mathcal{F}[a]$ to a fixed value a . ^(b) Inferred parameters and errors are defined as the median and 68.3% credible interval of the posterior distribution. ^(c) Assuming albedo = 0. ^(d) Calculated from the scaled-parameters as in Southworth et al. (2007).

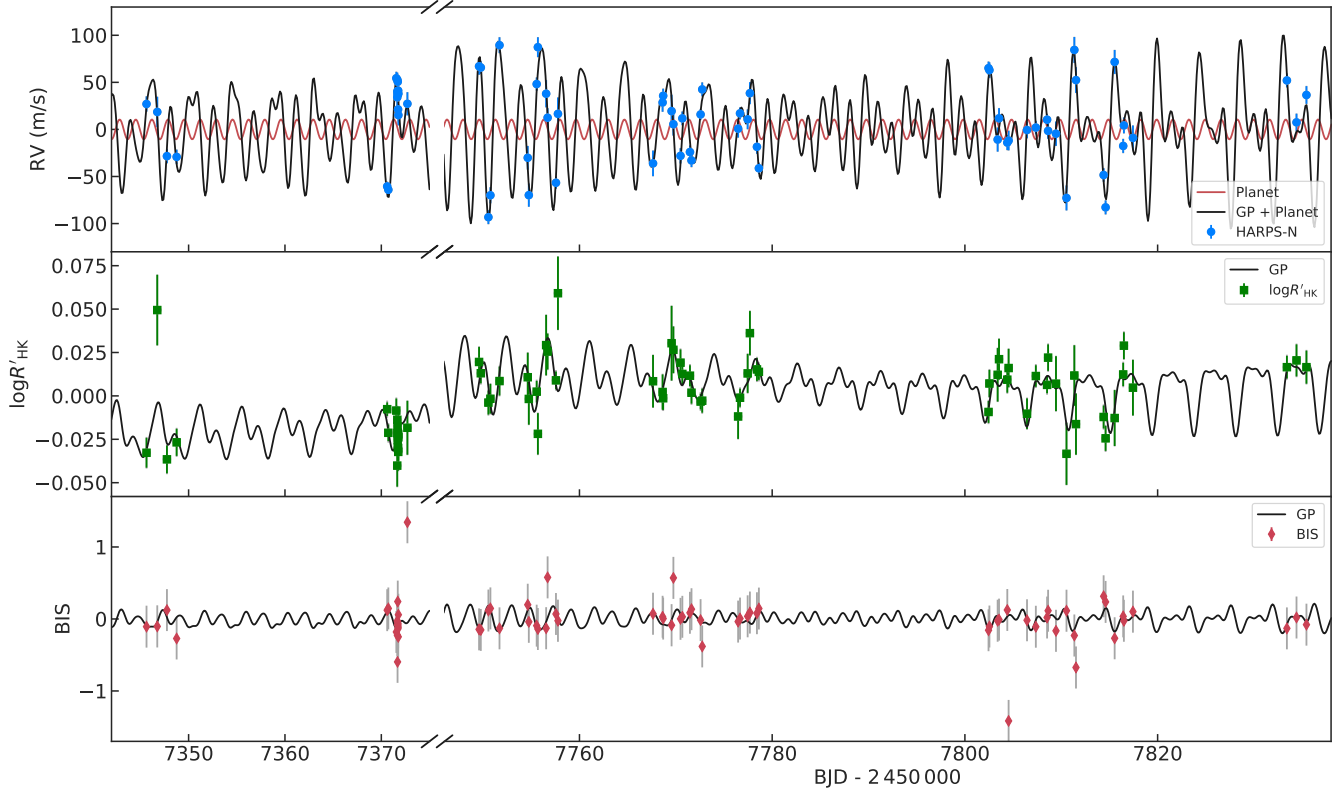


Figure 2. Radial velocity (top), $\log R'_{\text{HK}}$ (middle) and BIS (bottom) time-series. All time-series have been corrected by the inferred offset. Inferred models are presented as solid continuous lines. Measurements are shown with filled symbols with error bars. Grey error bars account for the jitter. We note that there is a gap between 7375 and 7746 BJD - 2 450 000 where there were no measurements.

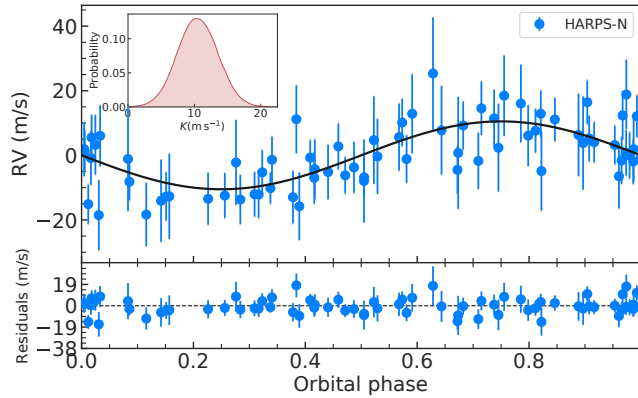


Figure 3. RV curve of K2-100 folded to the orbital period of K2-100b. HARPS-N data (blue circles) are shown following the subtraction of the instrumental offset and GP model. Grey error bars account for the jitter. The Keplerian solution is shown as a solid line. Top-left inset displays the posterior distribution for K .

with a solid core with a significant volatile envelope. Figure 6 also shows all highly irradiated small planets from Figure 5. We find that all relatively low mass ($\leq 10M_{\oplus}$) planets have densities higher than that of the Earth and they are consistent with a composition made of different mixtures of iron and silicates. This can be explained by the fact that close-in, low-mass planets beyond this insolation limit are expected to lose their primordial H/He atmospheres (e.g., Lundkvist et al. 2016). For planets with higher masses ($> 10M_{\oplus}$), instead, bulk densities are typically lower than that of the Earth

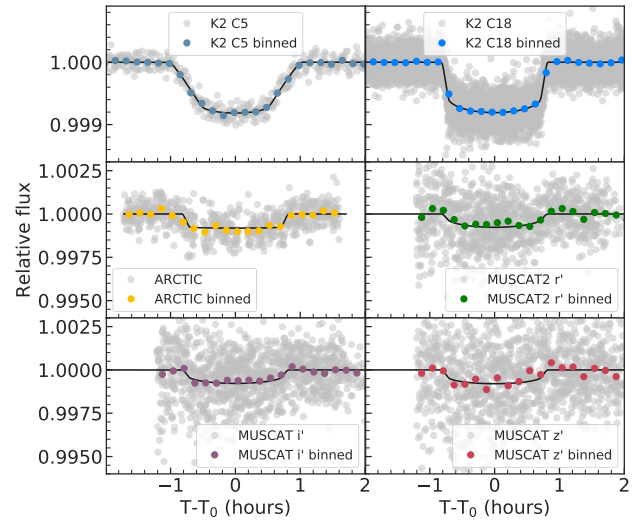


Figure 4. K2-100b transits. Each panel shows a flattened light curve from different instruments folded to the orbital period of K2-100b. Black lines show the best-fitting transit models.

and compositions range from mixes of silicates and water to solid cores with volatile envelopes. In fact, West et al. (2019) argue that NGTS-4b's relative low density may be caused by a relatively high core mass, which enables the planet to retain a significant volatile envelope.

Given the system's youth and short orbital separation, we

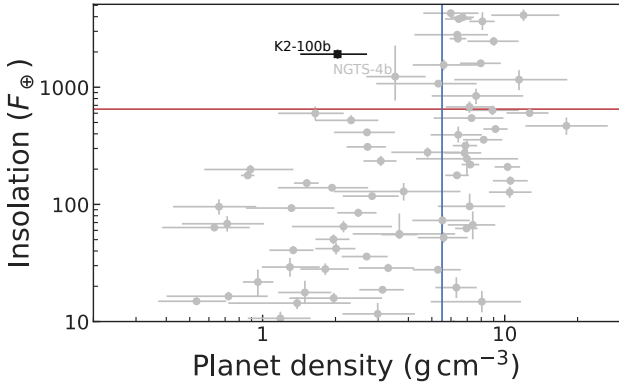


Figure 5. Planet density vs insolation for small ($R_p < 4 R_\oplus$) transiting planets (grey circles). The location of K2-100b is marked with a black square. We also label NGTS-4b. Horizontal red line shows the insolation limit of $650 F_\oplus$ given by Lundkvist et al. (2016). Vertical blue line corresponds to Earth’s density.

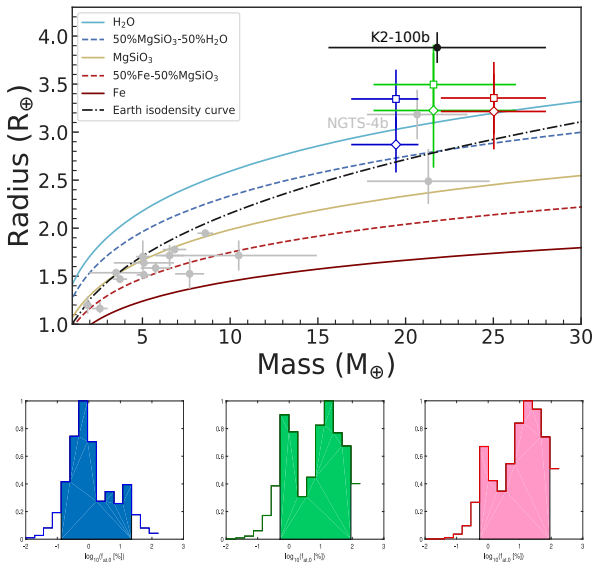


Figure 6. Top: Mass vs radius diagram for small ($R_p < 4 R_\oplus$) planets which receive an insolation > 650 larger than the Earth (grey circles). The location of K2-100b is marked with a black circle. Its predicted planetary mass and radius at 2 and 5 Gyr is shown with empty squares and diamonds, respectively, with colours corresponding to different initial rotation rates XUV fluxes for the star: fast/high (red), moderate (green) and slow/low (blue) (see text for details). Zeng et al. (2016)’s composition models are displayed with different colour lines. Bottom: posterior distributions obtained for the initial atmospheric mass fraction $f_{at,0}$ assuming the three different regimes of evolution of the stellar XUV flux. The shaded areas correspond to the 68% region of the credible interval of the posterior distribution.

model the past and future planetary atmospheric evolution, in particular to estimate if (and when) the planet will lose its envelope. To this end, we employed the planetary atmospheric evolution scheme described by Kubyskhina et al. (2018b, 2019, hereafter K18b and K19, respectively). This is based on a combination of model grids and analytical approximations. They comprise models providing atmospheric mass-loss rates as a function of system parameters (K18b), models enabling to estimate the atmospheric mass fraction as a function of planetary parameters (i.e., radius, mass, equilibrium temperature; Johnstone et al. 2015), and the Mesa/MIST grid

of stellar evolutionary tracks to account for the evolution of the stellar bolometric luminosity (Choi et al. 2016). We model the past and future evolution of the stellar rotation period using a prescription similar to the empirical period-colour-age relation of Mamajek & Hillenbrand (2008), modified to match the present-day rotation period, but with a free parameter x allowing us to vary the spin-down rate prior to 2 Gyr (see K19, for details). The instantaneous high-energy X-ray+EUUV (XUV) emission of the host star is estimated from the rotation period following Wright et al. (2011), allowing us to explore a wide range of scenarios for the integrated XUV budget of the planet over its lifetime.

As described in K19, we apply a Monte Carlo approach to fit the observed planetary radius, using the other system parameters and their uncertainties as inputs, finally obtaining probability distribution functions for x and the initial atmospheric mass fraction (i.e., ratio between atmospheric mass and planetary mass at an age of 5 Myr; $f_{at,0}$) as output. Altogether, the input parameters of the Monte Carlo simulation are planetary mass, orbital separation, age of the system, stellar mass, and present-day rotation period¹. We then use the results to evolve the planetary atmosphere beyond its current age and up to 5 Gyr, computing the planetary radius and f_{at} as a function of age and for three different ranges of x corresponding to rotation rates at an age of 150 Myr of less than 0.5 days, between 0.5 and 3 days, and more than 3 days. At an age of 150 Myr, these rotation rates translate to XUV fluxes in the range 376–600, 117–376, and 13–117 times larger than the current solar XUV emission, respectively. Throughout, we assume a core density equal to Earth’s bulk density, which sets the core radius.

Figure 6 shows the current position of the planet in the mass-radius diagram and those predicted to be possible at 2 and 5 Gyr, for the three different ranges of x we considered. Our results indicate that after 5 Gyrs the planet is likely to lose a significant amount of its primordial hydrogen-dominated atmosphere, finally retaining between about 0.1 and 0.7% of its mass in the atmosphere, depending on the evolutionary path of the stellar XUV emission and on planetary mass. In particular, for a planetary mass below about $20 M_\oplus$ it is unlikely that the planet will retain more than 0.1% of its mass in the atmosphere and therefore its predicted radius at 5 Gyr is close to the assumed core radius. In some cases, when considering planetary masses below $\sim 18 M_\oplus$, we reach the (almost) complete escape of the primary atmosphere before 2 Gyr.

In case the actual planetary mass is above about $20 M_\oplus$, the planet could still keep up to 0.7% of its mass in the atmosphere, as shown in Fig. 6. This plot shows that if K2-100 evolves as described by our fast rotator model, K2-100b should have a relatively high core mass, which is able to retain a significant volatile envelope. This could be similar to the case of NGTS-4b. On the other extreme, if K2-100 evolves as a slow rotator, which is possible if the planet has a mass closer to the lower mass limit given by the RV measurements, K2-100b would end up as a core with an Earth-like density, similar to the other highly irradiated planets.

As shown by K19, and illustrated on Figure 6, for a given stellar evolution scenario, the observed present-day radius of the planet can only be matched for a certain range of masses, which is within the mass range allowed (at the 1-sigma level) by our

¹ The planetary equilibrium temperature, which is one of the input parameters for extracting the mass-loss rates (by setting the lower boundary of the hydrodynamic modelling) and atmospheric mass fractions from the grids, is set by the orbital separation and stellar parameters, where the latter are derived from the MESA evolutionary tracks and the stellar mass.

RV results. We were unable to fit the observed present-day radius with any atmospheric evolution scenario for planet masses below $\sim 15 M_{\oplus}$: at such low planetary masses, the atmosphere essentially escapes entirely before the age of Praesepe, even if we assume that the initial stellar XUV flux was rather low.

Figure 6 also presents the posterior distributions we obtained for the initial planetary atmospheric mass fraction $f_{\text{at},0}$ for the three different ranges of x we considered. Larger XUV fluxes imply that more atmosphere has already escaped, so that the initial atmospheric mass fraction must have been larger (though the range of allowed values is also larger). Our results indicate that the planet may be subject to substantial atmospheric escape throughout most of its lifetime with the strongest escape happening during the first few hundred Myrs. In particular, for masses larger than about $20 M_{\oplus}$ atmospheric escape remains significant for Gyrs, implying that the planetary radius will keep decreasing, hence evolving, also after the first few hundred Myrs during which the planetary radius can decrease dramatically.

In all of the models that fit the available data, the planet is currently hosting an escaping atmosphere: using the code described by K18b, we computed a series of hydrodynamic models of the planetary upper atmosphere for the range of planet parameters spanned by the evolution models that fit the observational constraints. These yield present-day atmospheric mass-loss rates in the range 10^{11} – 10^{12} g s^{-1} .

5 CONCLUSIONS

We showed how, by combining RV with activity indicators, we can disentangle planetary and activity RV variations for young active stars. These results encourage the RV follow-up of young or active stars to be discovered with missions such as *TESS* and *PLATO*.

We measured a mass of $21.8 \pm 6.2 M_{\oplus}$ for K2-100b, a $3.88 \pm 0.16 R_{\oplus}$ planet transiting a star in the Praesepe cluster. We estimated that the relative high irradiation received by the planet implies that its atmosphere is currently evaporating. This makes K2-100 an excellent laboratory to test photo-evaporation models.

ACKNOWLEDGMENTS

This paper includes data collected by the K2 mission. Funding for the K2 mission is provided by the NASA Science Mission Directorate. Based on observations made with the Italian Telescopio Nazionale Galileo (TNG) operated on the island of La Palma by the Fundación Galileo Galilei of the INAF (Istituto Nazionale di Astrofisica) at the Spanish Observatorio del Roque de los Muchachos of the Instituto de Astrofísica de Canaria. Data for this paper has been obtained under the International Time Programme of the CCI (International Scientific Committee of the Observatorios de Canarias of the IAC). This article is based on observations made with the MuSCAT2 instrument, developed by ABC, at Telescopio Carlos Sánchez operated on the island of Tenerife by the IAC in the Spanish Observatorio del Teide. These results are based on observations obtained with the Apache Point Observatory 3.5-meter telescope, which is owned and operated by the Astrophysical Research Consortium. O.B. and S.Ai. acknowledge support from the UK Science and Technology Facilities Council (STFC) under grants ST/S000488/1 and ST/R004846/1. J.K., S.G. and A.P.H. acknowledges support by Deutsche Forschungsgemeinschaft (DFG) grants PA525/18-1 and PA525/19-1 and HPA 3279/12-1 within the DFG Schwerpunkt SPP 1992, Exploring the Diversity of Extra-solar Planets. L.M. acknowledges support

from PLATO ASI-INAF agreement n.2015-019-R.1-2018. S.Ai. acknowledges the support from the Danish Council for Independent Research through the DFF Sapere Aude Starting Grant No. 4181-00487B, and the Stellar Astrophysics Centre which funding is provided by The Danish National Research Foundation (Grant agreement no.: DNR106). This work is partly supported by JSPS KAKENHI Grant Numbers JP18H01265, JP18H05439, 15H02063, and 18H05442 and JST PRESTO Grant Number JPMJPR1775. M.C.V.F. and C.M.P. gratefully acknowledge the support of the Swedish National Space Agency (DNR 174/18).

REFERENCES

- Adams F. C., Laughlin G., 2006, *ApJ*, **649**, 1004
Aigrain S., Pont F., Zucker S., 2012, *MNRAS*, **419**, 3147
Barragán O., Gandolfi D., 2017, Exotrending (ascl:1706.001)
Barragán O., et al., 2018a, *MNRAS*, **475**, 1765
Barragán O., et al., 2018b, *A&A*, **612**, A95
Barragán O., Gandolfi D., Antoniciello G., 2019, *MNRAS*, **482**, 1017
Boesgaard A. M., Roper B. W., Lum M. G., 2013, *ApJ*, **775**, 8
Bossini D., et al., 2019, *A&A*, **623**, A108
Brandt T. D., Huang C. X., 2015, *ApJ*, **807**, 24
Bressan A., Marigo P., Girardi L., Salasnich B., Dal Cero C., Rubele S., Nanni A., 2012, *MNRAS*, **427**, 127
Bruntt H., et al., 2010, *MNRAS*, **405**, 1907
Burnham K., Anderson D., 2002, Model Selection and Multimodel Inference: A Practical Information-Theoretic Approach. New York: Springer-Verlag
Choi J., Dotter A., Conroy C., Cantiello M., Paxton B., Johnson B. D., 2016, *ApJ*, **823**, 102
David T. J., et al., 2016a, *AJ*, **151**, 112
David T. J., et al., 2016b, *Nature*, **534**, 658
David T. J., et al., 2019, *AJ*, **158**, 79
Doyle A. P., Davies G. R., Smalley B., Chaplin W. J., Elsworth Y., 2014, *MNRAS*, **444**, 3592
Fridlund M., et al., 2017, *A&A*, **604**, A16
Gaia Collaboration et al., 2018, *A&A*, **616**, A1
Gandolfi D., et al., 2008, *ApJ*, **687**, 1303
Gandolfi D., et al., 2017, *AJ*, **154**, 123
Grünblatt S. K., Howard A. W., Haywood R. D., 2015, *ApJ*, **808**, 127
Haywood R. D., et al., 2014, *MNRAS*, **443**, 2517
Howell S. B., et al., 2014, *PASP*, **126**, 398
Jackson B., Greenberg R., Barnes R., 2008, *ApJ*, **678**, 1396
Johnstone C. P., et al., 2015, *ApJ*, **815**, L12
Kipping D. M., 2010, *MNRAS*, **408**, 1758
Kipping D. M., 2013, *MNRAS*, **435**, 2152
Kraus A. L., Hillenbrand L. A., 2007, *AJ*, **134**, 2340
Kubyskhina D., Lendl M., Fossati L., Cubillos P. E., Lammer H., Erkaev N. V., Johnstone C. P., 2018a, *A&A*, **612**, A25
Kubyskhina D., et al., 2018b, *A&A*, **619**, A151
Kubyskhina D., et al., 2019, *ApJ*, **879**, 26
Kurucz R. L., 2013, ATLAS12 (ascl:1303.024)
Libralato M., et al., 2016, *MNRAS*, **463**, 1780
Lightkurve Collaboration et al., 2018, Lightkurve: Kepler and TESS time series analysis in Python (ascl:1812.013)
Livingston J. H., et al., 2018a, *AJ*, **155**, 115
Livingston J. H., et al., 2018b, *AJ*, **156**, 277
Livingston J. H., et al., 2019, *MNRAS*, **484**, 8
Lundkvist M. S., et al., 2016, *Nature Communications*, **7**, 11201
Malavolta L., et al., 2018, *AJ*, **155**, 107
Mamajek E. E., Hillenbrand L. A., 2008, *ApJ*, **687**, 1264
Mann A. W., et al., 2016a, *AJ*, **152**, 61
Mann A. W., et al., 2016b, *ApJ*, **818**, 46
Mann A. W., et al., 2017, *AJ*, **153**, 64
Mann A. W., et al., 2018, *AJ*, **155**, 4
Mermilliod J. C., 1987, *A&AS*, **71**, 413
Morton T. D., 2012, *ApJ*, **761**, 6

- Narita N., et al., 2019, *Journal of Astronomical Telescopes, Instruments, and Systems*, 5, 015001
- Owen J. E., Wu Y., 2013, *ApJ*, 775, 105
- Pace G., Pasquini L., François P., 2008, *A&A*, 489, 403
- Parviainen H., 2015, *MNRAS*, 450, 3233
- Parviainen H., Aigrain S., 2015, *MNRAS*, 453, 3822
- Parviainen H., et al., 2019, arXiv e-prints, p. arXiv:1907.09776
- Pecaut M. J., Mamajek E. E., 2013, *ApJS*, 208, 9
- Pepe F., et al., 2013, *Nature*, 503, 377
- Pepper J., et al., 2017, *AJ*, 153, 177
- Persson C. M., et al., 2018, *A&A*, 618, A33
- Petigura E. A., et al., 2015, *ApJ*, 811, 102
- Piskunov N., Valenti J. A., 2017, *A&A*, 597, A16
- Pope B. J. S., Parviainen H., Aigrain S., 2016, *MNRAS*, 461, 3399
- Rajpaul V., Aigrain S., Osborne M. A., Reece S., Roberts S., 2015, *MNRAS*, 452, 2269
- Rajpaul V., Aigrain S., Roberts S., 2016, *MNRAS*, 456, L6
- Raymond S. N., Barnes R., Veras D., Armitage P. J., Gorelick N., Greenberg R., 2009, *ApJ*, 696, L98
- Ryabchikova T., Piskunov N., Kurucz R. L., Stempels H. C., Heiter U., Pakhomov Y., Barklem P. S., 2015, *Phys. Scr.*, 90, 054005
- Salaris M., Weiss A., Percival S. M., 2004, *A&A*, 414, 163
- Southworth J., 2011, *MNRAS*, 417, 2166
- Southworth J., Wheatley P. J., Sams G., 2007, *MNRAS*, 379, L11
- Stefansson G., Li Y., Mahadevan S., Wisniewski J., Hebb L., Morris B., Huehnerhoff J., Hawley S., 2018, *AJ*, 156, 266
- Valenti J. A., Piskunov N., 1996, *A&AS*, 118, 595
- Vanderburg A., Johnson J. A., 2014, *PASP*, 126, 948
- West R. G., et al., 2019, *MNRAS*, 486, 5094
- Winn J. N., 2010, arXiv e-prints, p. arXiv:1001.2010
- Wright N. J., Drake J. J., Mamajek E. E., Henry G. W., 2011, *ApJ*, 743, 48
- Yee S. W., Petigura E. A., von Braun K., 2017, *ApJ*, 836, 77
- Zeng L., Sasselov D. D., Jacobsen S. B., 2016, *ApJ*, 819, 127
- van Leeuwen F., 2009, *A&A*, 497, 209

APPENDIX A: HARPS-N MEASUREMENTS

This paper has been typeset from a $\text{\TeX}/\text{\LaTeX}$ file prepared by the author.

Table A1. Radial velocity, activity and symmetry indicators measurements for K2-100.

Time (BJD _{TDB} -2,450,000)	RV (km s ⁻¹)	σ_{RV} (km s ⁻¹)	CCF BIS (km s ⁻¹)	CCF FWHM (km s ⁻¹)	$\log R'_{HK}$	$\sigma_{\log R'_{HK}}$	S/N
7345.63288	34.4200	0.0080	21.1143	-0.1473	-4.4804	0.0086	51.3
7346.74932	34.4116	0.0161	20.8156	-0.1438	-4.3982	0.0203	28.1
7347.75251	34.3646	0.0074	20.8381	0.0827	-4.4842	0.0080	54.2
7348.75941	34.3638	0.0076	20.9736	-0.3119	-4.4744	0.0078	54.2
7351.70898	34.0950	0.0453	21.1253	0.6314	-4.3827	0.0741	11.3
7351.73144	33.6321	0.1215	24.0350	1.0506	-3.9538	0.1979	2.3
7352.72840	34.1035	0.0536	21.8887	0.4047	-4.4255	0.1046	9.1
7352.74247	33.7331	0.0485	23.0619	2.5142	-4.2920	0.0653	10.4
7370.61016	34.3325	0.0048	20.7341	0.0814	-4.4553	0.0039	82.2
7370.72940	34.3289	0.0054	20.7907	0.1057	-4.4689	0.0048	70.9
7371.55846	34.4474	0.0067	20.7710	-0.2209	-4.4561	0.0069	60.1
7371.65315	34.4271	0.0100	20.8869	-0.0685	-4.4878	0.0121	42.4
7371.66420	34.4457	0.0075	20.8768	-0.2659	-4.4614	0.0075	53.3
7371.67486	34.4338	0.0070	20.9119	-0.1224	-4.4692	0.0069	56.4
7371.68506	34.4326	0.0071	20.8996	-0.6367	-4.4650	0.0070	55.3
7371.69614	34.4302	0.0069	21.0014	-0.0799	-4.4731	0.0067	57.4
7371.70673	34.4437	0.0064	20.9632	0.2011	-4.4688	0.0060	60.7
7371.71745	34.4300	0.0065	20.9909	-0.1295	-4.4773	0.0062	60.6
7371.72832	34.4315	0.0065	20.9366	-0.1761	-4.4703	0.0064	59.7
7371.73898	34.4143	0.0060	20.9340	-0.1083	-4.4778	0.0056	64.6
7371.74885	34.4342	0.0069	21.0073	-0.1534	-4.4696	0.0068	57.3
7371.76023	34.4309	0.0092	21.0583	-0.2884	-4.4799	0.0108	44.6
7371.77033	34.4082	0.0108	21.0351	0.0180	-4.4715	0.0135	38.6
7372.67782	34.2780	0.0548	20.2459	-0.0747	-4.3204	0.0816	9.3
7372.70837	34.4203	0.0122	20.6497	1.3029	-4.4660	0.0155	35.1
7749.58185	34.4601	0.0088	18.9395	-0.1852	-4.4281	0.0086	44.7
7749.76345	34.4587	0.0067	18.9701	-0.1929	-4.4346	0.0058	59.4
7750.55088	34.2998	0.0072	18.9979	0.0767	-4.4515	0.0069	57.0
7750.75882	34.3231	0.0084	18.8521	0.1063	-4.4493	0.0085	49.7
7751.70251	34.4825	0.0083	18.9755	-0.1709	-4.4391	0.0083	49.8
7754.63363	34.3629	0.0124	21.0214	0.1569	-4.4369	0.0141	32.8
7754.74514	34.3232	0.0122	20.9659	-0.0801	-4.4494	0.0148	34.6
7755.56052	34.4412	0.0068	20.3272	-0.1334	-4.4452	0.0062	58.3
7755.68564	34.4804	0.0105	20.6427	-0.1800	-4.4695	0.0119	40.5
7756.54391	34.4309	0.0144	20.9620	-0.1692	-4.4184	0.0174	31.2
7756.69497	34.4055	0.0100	21.1398	0.5372	-4.4221	0.0103	42.5
7757.56227	34.3364	0.0062	20.5935	0.0287	-4.4387	0.0051	64.3
7757.76849	34.4096	0.0173	20.5733	-0.0650	-4.3885	0.0211	26.6
7767.63488	34.3569	0.0135	20.6536	0.0321	-4.4392	0.0151	32.2
7768.62766	34.4216	0.0098	20.7994	-0.0101	-4.4454	0.0101	40.1
7768.68724	34.4287	0.0074	20.8263	-0.0352	-4.4490	0.0067	55.8
7769.56123	34.4124	0.0173	20.8606	-0.1276	-4.4173	0.0215	26.8
7769.74871	34.3985	0.0120	20.9550	0.5301	-4.4211	0.0134	36.7
7770.48664	34.3650	0.0080	20.7612	-0.0388	-4.4285	0.0076	51.3
7770.67781	34.4047	0.0071	20.6799	-0.0105	-4.4350	0.0065	56.8
7771.46646	34.3690	0.0067	21.0110	0.0454	-4.4360	0.0060	60.7
7771.62722	34.3601	0.0070	20.7487	0.0950	-4.4458	0.0063	57.5
7772.57081	34.4089	0.0055	20.5872	-0.0564	-4.4509	0.0045	71.3
7772.74143	34.4355	0.0073	20.5553	-0.4219	-4.4504	0.0069	57.2
7776.46636	34.3938	0.0094	20.8932	-0.0770	-4.4595	0.0129	47.7
7776.66380	34.4101	0.0062	20.7195	-0.0348	-4.4487	0.0052	65.2
7777.45522	34.4037	0.0104	20.8038	-0.0037	-4.4347	0.0112	41.2
7777.68914	34.4315	0.0116	20.5416	0.0484	-4.4115	0.0127	37.6
7778.41974	34.3745	0.0072	20.9883	0.0391	-4.4324	0.0066	57.8
7778.62073	34.3518	0.0057	20.7787	0.1042	-4.4338	0.0046	69.2
7802.45286	34.4581	0.0068	20.4947	-0.1972	-4.4569	0.0063	58.7
7802.54483	34.4560	0.0081	20.6486	-0.1455	-4.4405	0.0078	50.5
7803.39940	34.3822	0.0127	20.6459	-0.0650	-4.4355	0.0154	34.5
7803.54249	34.4048	0.0107	20.4169	-0.0496	-4.4265	0.0117	39.2

Table A1 – continued

Time (BJD _{TDB} -2,450,000)	RV (km s ⁻¹)	σ_{RV} (km s ⁻¹)	CCF BIS (km s ⁻¹)	CCF FWHM (km s ⁻¹)	$\log R'_{HK}$	$\sigma_{\log R'_{HK}}$	S/N
7804.40126	34.3790	0.0078	20.8478	0.0843	-4.4383	0.0075	52.5
7804.53623	34.3812	0.0103	20.6631	-1.4568	-4.4316	0.0110	40.8
7806.44739	34.3924	0.0087	20.5212	-0.0588	-4.4579	0.0088	47.8
7807.36241	34.3950	0.0069	21.3158	-0.1485	-4.4362	0.0062	59.0
7808.52958	34.4034	0.0059	21.0225	-0.0204	-4.4413	0.0048	68.2
7808.63565	34.3915	0.0082	20.9503	0.0738	-4.4256	0.0076	51.6
7809.45282	34.3884	0.0128	20.7297	-0.2052	-4.4406	0.0158	34.2
7810.54426	34.3202	0.0132	20.3217	0.0739	-4.4810	0.0179	33.4
7811.35884	34.4775	0.0137	20.7007	-0.2704	-4.4359	0.0174	32.9
7811.52928	34.4454	0.0136	21.1617	-0.7146	-4.4639	0.0176	31.8
7814.39794	34.3446	0.0070	21.1399	0.2747	-4.4598	0.0066	57.5
7814.60206	34.3102	0.0073	20.8498	0.1962	-4.4721	0.0072	57.4
7815.54132	34.4647	0.0127	20.7258	-0.3086	-4.4604	0.0161	34.7
7816.42836	34.3755	0.0074	20.5119	-0.0049	-4.4353	0.0067	54.8
7816.49993	34.3972	0.0083	20.5529	-0.0658	-4.4187	0.0077	50.1
7817.43947	34.3840	0.0131	21.0605	0.0611	-4.4429	0.0160	33.9
7833.41663	34.4450	0.0072	21.0347	-0.1712	-4.4311	0.0065	56.5
7834.41427	34.4005	0.0091	21.2186	-0.0202	-4.4272	0.0092	44.9
7835.44577	34.4296	0.0094	20.8092	-0.1197	-4.4311	0.0095	43.6